

Full paper



Conformal self-powered high signal-to-noise ratio biomimetic in-situ aircraft surface turbulence mapping system[☆]

Hengrui Sheng^{a,b,1}, Leo N.Y. Cao^{a,b,c,1}, Yurui Shang^{a,b,1}, Chengyu Li^a, Zhuyu Zhou^a, Yang Jiang^{a,b,c}, Yanshuo Sun^{a,b}, Wei Tang^{a,b,c}, Baodong Chen^{a,b,c}, Wenxi Guo^d, Zijie Xu^{a,b,c,*}, Zhong Lin Wang^{a,b,c,*} 

^a Beijing Key Laboratory of Micro-Nano Energy and Sensor, Center for High-Entropy Energy and Systems, Beijing Institute of Nanoenergy and Nanosystems, Chinese Academy of Sciences, Beijing 101400, China

^b School of Nanoscience and Technology, University of Chinese Academy of Sciences, Beijing 100049, China

^c Guangzhou Institute of Blue Energy, Knowledge City, Huangpu District, Guangzhou 510555, China

^d College of Physical Science and Technology, Xiamen University, Xiamen 361005, China

ARTICLE INFO

Keywords:

Self-powered sensing
Turbulence mapping
Distributed sensing
Triboelectric nanogenerator
Wireless transmission

ABSTRACT

Turbulence, a state of disordered and random air hydrodynamic phenomenon, constantly pits it against flight safety during aviation. In the interplay between safe flight and turbulence, the challenge of real-time in situ monitoring of the surface airflow state on aircraft has become a difficult but crucial challenge. However, due to constraints in materials science and technological advancements, a flawless solution for mapping the surface airflow of aircraft has not yet been developed. Herein, based on the strong conformability, strong positive triboelectric silk fibroin and fluid dynamics biomimetic design, a self-powered, high signal-to-noise ratio in-situ aircraft surface turbulence mapping system has been developed based on the principle of triboelectric nanogenerators (TENGs). On one hand, the system functions as a vortex generator during normal flight; on the other hand, the system can swiftly detect the degree of stall and enhance flight safety when the aircraft suffers airflow separation due to a high angle of attack. The backend signal of the system is transmitted by a self-developed wireless transmitter, suitable for various fixed-wing aircraft.

1. Introduction

Flight safety [1], the fundamental principle in flight aviation, is critical despite still full of challenges [2]. From the inception of the Reynolds number to the formulation of the Navier-Stokes equations [3, 4]; from the launch of the world's first aircraft [5], the Flyer, in 1903, to the supersonic aircraft a century later [6,7]; from the use of wood as the material for aircraft shells to the current high-performance composite aluminum alloy materials [8], human technological breakthroughs have driven the leapfrog development of aircraft safety. It is not difficult to see that the progress in materials and manufacturing techniques, coupled with the continuous advancement of industrial science and

technology, has progressively made aircraft the most efficient mode of human transportation.

As the aviation industry advances, flight safety sensing systems are progressing rapidly [9]. Yet, within this sector, the advancement of airflow sensing technology on aircraft surface, is still facing challenges due to the complexity of sensing methods and underlying principles, indicating substantial potential for further improvement [10]. In 2018 and 2019, two successive Boeing 737 MAX 8 air disasters within five months claimed 346 lives [11]. The cause of the accidents was directly attributed to erroneous commands from the stall system. On August 9, 2024, a Brazilian airliner crashed due to stalling, claiming another 62 lives. Perhaps it is time to start searching for a new technology that can

[☆] Prof Zhong Lin Wang, an author on this paper, is the former Editor-in-Chief of Nano Energy, but he had no involvement in the peer review process used to assess this work submitted to Nano Energy. This paper was assessed, and the corresponding peer review managed by Professor Chenguo Hu, also an Associate Editor in Nano Energy.

* Corresponding authors at: Beijing Key Laboratory of Micro-Nano Energy and Sensor, Center for High-Entropy Energy and Systems, Beijing Institute of Nanoenergy and Nanosystems, Chinese Academy of Sciences, Beijing 101400, China.

E-mail addresses: xuzijie@binn.cas.cn (Z. Xu), zhong.wang@mse.gatech.edu (Z.L. Wang).

¹ These authors contributed equally: H. Sheng, L. N. Y. Cao and Y. Shang.

<https://doi.org/10.1016/j.nanoen.2025.110694>

Received 12 December 2024; Received in revised form 13 January 2025; Accepted 19 January 2025

Available online 24 January 2025

2211-2855/© 2025 Elsevier Ltd. All rights are reserved, including those for text and data mining, AI training, and similar technologies.

more accurately monitor the airflow over the aircraft wing, thus warning of stall occurrence [12].

As the primary cause of air disasters worldwide, aerodynamic stall [13] due to wing surface airflow separation still lacks effective in-situ direct monitoring methods [14], and existing indirect monitoring technologies exhibit numerous issues [15]: (i) Environmental sensitivity. Optical Bragg sensors are vulnerable to external environmental influences, such as fluctuations in temperature and humidity, which may compromise their performance and stability [16]. (ii) Existence of error rate. Differential pressure sensors [17], utilized for measuring wind speed and airflow, are prone to inaccuracies due to contamination and potential blockages, which can cause sensor failure or erratic outputs [18]. (iii) Limited arraying. The limited space within aircraft imposes restrictions on sensor placement, making the deployment of multiple sensor arrays a challenging task due to spatial complexity [19]. (iv) Time delay. Sensor-gathered data is not available for immediate feedback [20] as it requires processing through a data model before utilization [21]. (v) Single function. The sensor only has the function of monitoring [22] and cannot be used as other functions [23]. In light of these limitations, the pursuit of new technologies and strategies is essential to bolster aircraft flight safety.

Here, to address these issues, we propose conformal self-powered high signal-to-noise ratio biomimetic in-situ aircraft surface turbulence mapping system. Through the optimization and innovation of silk fibroin materials, we employ them as strongly positively charged components within a self-powered sensing system, paired with negatively charged materials to effectively enhance the system's signal-to-noise ratio (56.21 dB) [24,25]. Additionally, the triboelectric nanogenerator (TEENG) technology allows the system to operate stably and independently [26–30], streamlining the front-end sensing structure and eliminating the need for complex power and circuitry systems. Furthermore, aerodynamic design enables ultrafast response (4 ms) to stall occurrences during in situ monitoring of airflow conditions on the wing surface. Lastly, the biomimetic [31,32] vortex generator (VG) at the front end provides stall signals and helps delay the onset of stall [33].

Moreover, we have developed a set of self-developed wireless transmission equipment. This equipment uses a 433 MHz antenna transmission, compared to Bluetooth and WiFi transmissions, 433 MHz antennas offer low power, long transmission distance, and weak signal attenuation. 433 MHz antenna combined with aircraft VG [34], arrayed monitoring of different airfoil regions becomes possible. Through multi-area calibration, flight safety is ensured more stably. In summary, the advent of the in-situ aircraft surface turbulence mapping system (ASTMS), rooted in materials science and leveraging principles from aerodynamics and fluid mechanics [35,36], along with triboelectric charge separation technology, enables the in situ, real-time, and self-powered mapping of the surface airflow on aircraft wings.

2. Results and discussion

2.1. The working mechanism of the in-situ aircraft surface turbulence mapping system (ASTMS)

Flight safety is a fundamental principle in aviation, and achieving this goal is fraught with complexity and numerous challenges. During the evolution of aircraft development, although progress has been made in improving flight safety, one of the most important factors affecting flight safety, stall, has not yet been effectively addressed [13]. To ensure higher flight safety, it has been theorized that higher Reynolds numbers (Eq. 1) can reduce the occurrence of stall [37,38].

$$\text{Re} = \frac{\rho v L}{\mu} \quad (1)$$

Where ρ denotes the fluid density, v denotes the velocity of the flow field, L is the main dimension of the object, and μ is the coefficient of

viscosity.

The purpose of this study is dedicated to ensuring flight safety by monitoring the aircraft surface turbulence mapping. Stall is a threat to flight safety due to the separation of airflow at the aircraft surface and the occurrence of reverse turbulence, which leads to a reduction in lift and an increase in drag of the aircraft [39,40]. For this reason, an ASTMS with biomimetic structure and composed of strongly positive tribomaterials has been designed to monitor surface airflow changes. The overall length of the ASTMS is 92 mm (Fig. S1), and the weight is only 10.55 g (Fig. S2). The ASTMS consists of three main components: the VG, the active electrode, and the static electrode. The VG is placed on the surface of the airfoil, which controls the airflow and delays airflow separation (Fig. S3). The active electrode consists of a steel sheet and fluorinated ethylene propylene (FEP), while the stationary electrode consists of copper and silk fibroin (SF) film. And according to the features of manta rays, the biomimetic structure shown in Fig. 1 is designed, which can control the air flow and delay the separation point of the airflow.

The operating principle of the ASTMS is based on the TENG technique and has aerodynamic ultrafast response that utilizes the reverse turbulence at stall to achieve stall monitoring. When the airflow on the aircraft surface is laminar flow (Fig. S4a), the active electrode is that the pressure difference between the upper and lower surfaces is less than the gravity of the electrode (Fig. S5a and Eq. 2), which keeps the active electrode in a stationary state. And when the airflow on the aircraft surface is turbulence flow (Fig. S4b), the reverse turbulence acts on the active electrode, and the pressure difference acting on the active electrode at this time is larger than the gravity of the electrode (Fig. S5b and Eq. 3). Under the action of the reverse turbulence, the active electrode starts to vibrate, contacts and separates from the stationary electrode, and generate a sensing signal, which realizes the monitoring of the aircraft surface turbulence flow. In addition, in order to prevent the problem of stall signal not being transmitted due to the damage of the transmission line, we have self-developed a wireless transmission device, which utilizes a 433 MHz antenna to transmit the stall signal to the cockpit, to ensure that the signal is transmitted reliably.

$$F_1 = \Delta P_1 \times S < G \quad (2)$$

$$F_2 = \Delta P_2 \times S > G \quad (3)$$

Where the number 1 is the laminar flow, and 2 is the turbulence flow. F is the force acting on the active electrode, P is the difference in pressure between the upper and lower surfaces of the active electrode, S is the area of the airflow acting on the active electrode, and G is the gravitational force of the active electrode.

In summary, the ASTMS has the following advantages in monitoring aircraft surface turbulence mapping: (i) it can monitor in-situ the generation of reverse turbulence during a stall; (ii) it adopts non-invasive self-powered sensors without the need for external energy supply; (iii) it is a multifunctional sensor with airflow control which is a biomimetic structure based on manta ray and digitized sensing; and (iv) it is capable of monitoring sensors at different locations to achieve arrays of sensing.

2.2. Optimization of ASTMS tribomaterials

As a pivotal element in the realm of science and technology, a sensor's performance [41] is inherently tied to the material from which it is crafted [42]. Therefore, the selection and stability of the sensor material [43] play a critical role in determining the sensor's overall performance and reliability [44]. Beyond having a basic output capability, sensor materials must exhibit resilience in specific environmental conditions, including high and low temperatures, humidity, chemical corrosion, and other extreme surrounding, to uphold performance and accuracy. Drawing upon the attributes of triboelectricity and building upon our previous research, we opted for the use of modified SF material with outstanding performance as the tribomaterial for the ASTMS integrated

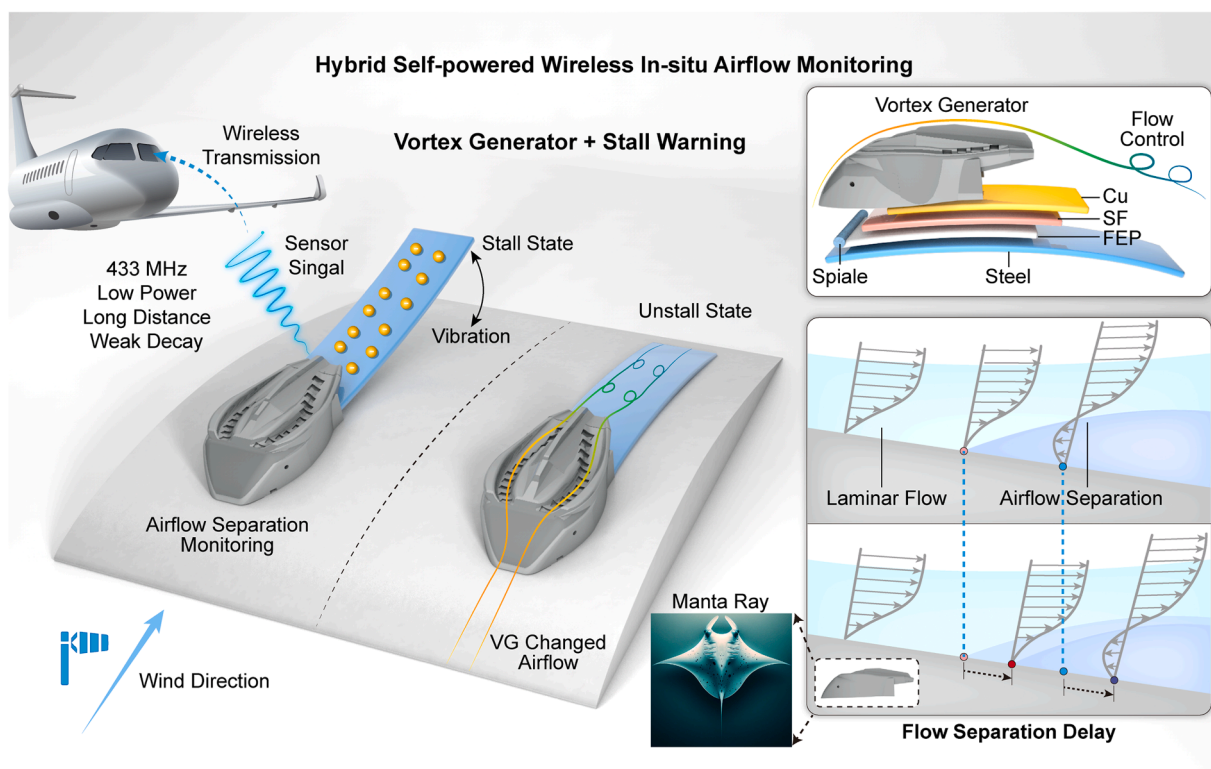


Fig. 1. Schematic diagram of the working principle and structure of in situ aircraft surface turbulence mapping system (ASTMS). The VG is hybridized with the sensor, and when there is laminar flow, the VG controls the airflow on the airfoil and the airflow separation point is delayed; when there is a turbulence flow, the sensor works to generate a sensing signal and wirelessly transmits the stall signal to the cockpit through the 433 MHz band.

aircraft surface.

SF [45,46] is a special material extracted from natural silkworm cocoons and processed through a series of processes (see previous work for detailed steps) [47]. This material has excellent conformal and can be bent and folded at will (Fig. S6), and the SF film is only 40 μm thick (Fig. S7). It is worth noting that SF is a strongly positive material when used as a tribomaterial, and a higher electrical signal can be obtained when in contact with a negative material (Fig. 2a). Infrared spectroscopic testing of the SF material revealed characteristic peaks associated with the β -sheet structure (Fig. 2b), indicating a transformation in the structure of the prepared SF material towards a more stable β -sheet structure.

Considering the specific operational conditions of the ASTMS integrated aircraft surface, utilizing SF as the tribomaterial offers several notable advantages: (i) Corrosion resistance. SF material demonstrates corrosion resistance when subjected to a pH range of 4–9, as evidenced by infrared spectroscopy testing (Fig. S8, Supporting Information). There was no significant alteration in the characteristic peaks during this test (Fig. 2c). (ii) Temperature resistance. Given the varied operating temperatures experienced by ASTMS during irregular flight environments and aircraft timings, SF material was simulation ranging from -30°C to 60°C . Infrared spectroscopy testing showed no significant change in the characteristic peaks under these conditions (Fig. 2d). At the same time, the output performance of FEP and SF films is robust in different temperature and pH environments (Figs. S9 to S11). (iii) High flatness. Employing one of the contact separation modes, where materials with higher flatness provide more contact area. ASTMS benefits from the excellent surface flatness of the SF material (10 mm \times 10 mm), evident in the atomic force microscopy (AFM) test with an R_q value of 1.212 nm (Fig. 2e). (iv) Hydrophobicity. Recognizing the potential impact of water droplets on sensor performance in aircraft operating at varying altitudes and ambient humidity levels. The SF material underwent surface treatment, achieving a water droplet contact angle

exceeding 130° (Fig. 2f). The hydrophobically treated SF film avoids the influence of external wetting environment on ASTMS. (v) Strongly positive. Achieving a higher signal-to-noise ratio (SNR) enhances the stability of the sensed signal. SF material, with a highly positive charge, in contact with FEP material, produces a higher voltage signal (Fig. 2g and Figs. S12 and S13).

In conclusion, the outstanding corrosion resistance, temperature resistance, and hydrophobicity exhibited by SF make it well-suited for a variety of flight environments. Additionally, the combination of high flatness and a highly positive charge positions the ASTMS acquire superior and stable sensing signals. As a result, SF was chosen as the ideal tribomaterial for monitoring airflow on the aircraft's surface.

2.3. Performance testing for ASTMS standardization

Where different material surfaces exhibit varying capacities for electric charge binding. During operation, when SF and FEP materials come into contact, SF is more prone to losing electrons, resulting in a positive surface charge. While FEP is inclined to gain electrons, leading to a negative surface charge. Upon separation of the two materials, due to electrostatic induction, where the conductive electrode on the back side induces a charge opposite to that of the surface electrode. By connecting the conducting electrodes, during each contact and separation cycle, the charge moves between the two electrodes due to the triboelectric effect and electrostatic induction, generating an electrical signal (Fig. S14). Simulations of the surface potential during contact separation (Fig. 3a) reveal that the surface potential is maximum when the two electrodes are completely separated and minimum when they are in full contact.

In order to evaluate the output performance of the developed ASTMS, standardized validation experiments were conducted with a linear motor to verify its basic electrical performance output (Fig. 3b). These experiments are essential to verify the feasibility of the proposed

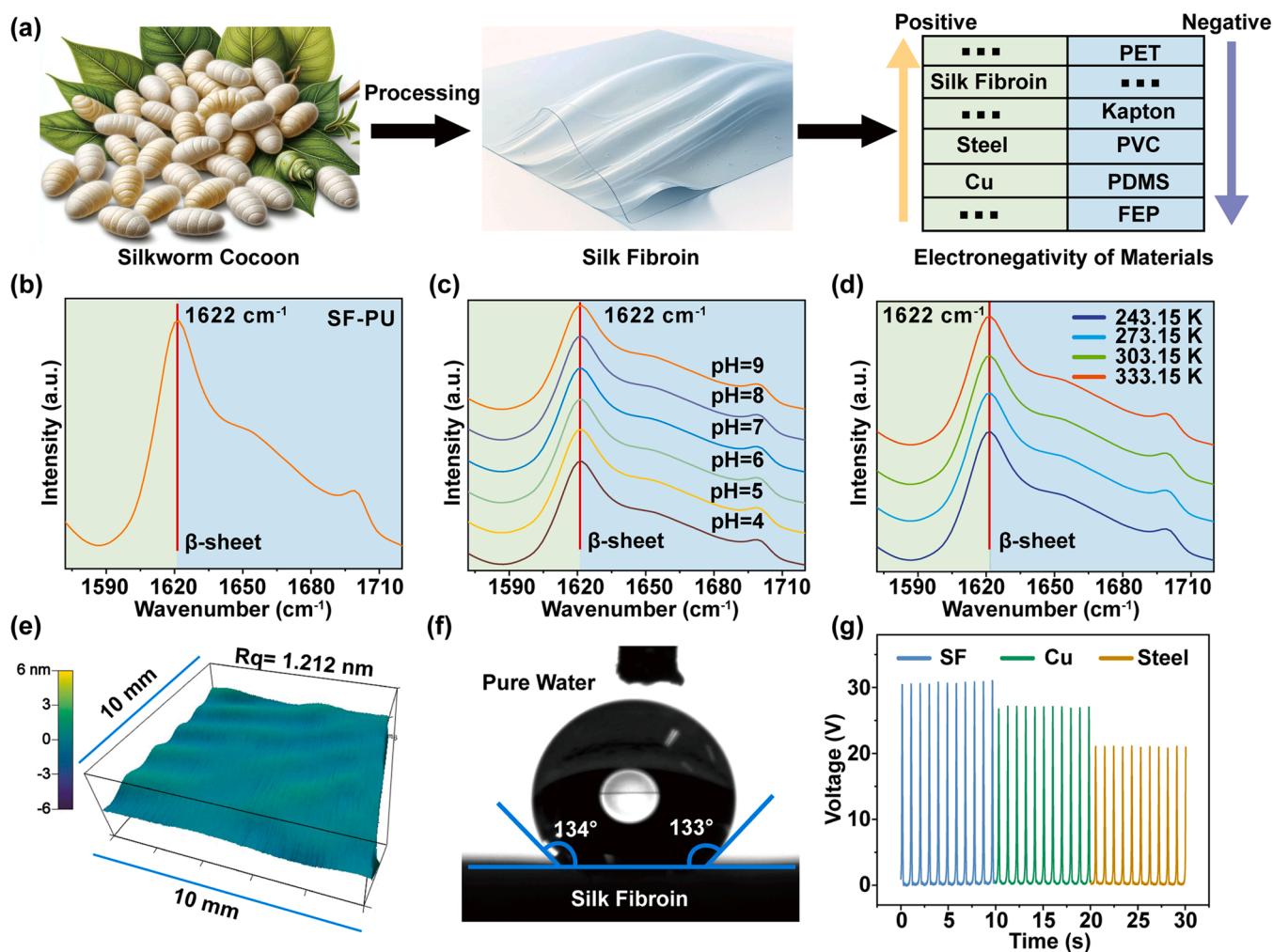


Fig. 2. Characterization testing of SF material properties. (a) SF is prepared from silkworm cocoons and has a strong positive tribomaterial. (b) Infrared spectrum testing of SF with characteristic peak. (c) Infrared spectra of SF in environments from pH 4–9. (d) Infrared spectra of SF at temperatures from -30° to 60° . (e) Surface flatness of SF under AFM test. (f) Surface-treated SF has high hydrophobicity. (g) The voltage output of SF material is compared with that of steel and copper.

theory (Fig. 3c and d). SF has excellent properties as a tribomaterial, which can generate voltages up to 70 V, currents up to 1.25 μ A, and transfer charges up to 30 nC. Therefore, high voltages are selected as the output of sensing signals. The high-output sensing signal exhibits a commendable SNR, effectively mitigating the risk of misjudgment induced by external interferences. Furthermore, ASTMS showcases exceptional continuous operation capability. The voltage output remains consistently high, exhibiting minimal drop even after enduring 130,000 cycles. This indicates that ASTMS not only meets the daily operational demands of aircraft but also maintains excellent sensing capability even after prolonged use.

A comprehensive series of standardized experiments were undertaken to simulate the operational conditions of the system integrated aircraft surface and validate its exceptional sensing capabilities. The system can operate self-powered in the presence of turbulence flow on the aircraft surface. But the state of the turbulence flow is chaotic, and likewise the movement of the active electrodes is irregular, which results in the distance, frequency, and the active electrodes at the time of contact pressure is unpredictable. Despite these uncertainties, the ability of ASTMS to maintain its superior sensing capabilities needs to be verified. To address this, we conducted simulations of different motion states of the active electrodes under the influence of the separating airflow using a linear motor: (i) Varied travel distances. Keeping motor speed and acceleration constant ($v=0.5 \text{ m s}^{-1}$, $a=0.5 \text{ m s}^{-2}$) for different travel distances, has a high output capability (Fig. 3e–h and

Fig. S15). Stable sensing signal output remains available at shorter movement distances. (ii) Diverse movement frequencies. By controlling the linear motor frequency of motion (100 mm to 162.3 mm), the electrical output performance increased with higher movement frequencies (Fig. 3f–i and Fig. S16). The ASTMS maintains a stable sensing capability at higher operating frequencies. (iii) Varying contact pressures. The stationary electrode was affixed to the manometer, and the maximum pressure experienced by the manometer was recorded at each instance. The output performance exhibited an increase with rising pressure but stabilized with further pressure increase (Fig. 3g–j and Fig. S17). Additionally, the system has the potential for energy harvesting where necessary (Fig. S18).

In conclusion, the results of standardized tests on linear motors show that the system has excellent capabilities. The system provides basic capability, sustained operational efficiency, and sensing capability under different states of motion as caused by the separation of airflow. These results indicate that the ASTMS can effectively meet the requirements for monitoring airflow conditions.

2.4. ASTMS cyclic wind tunnel testing and optimization

Standardized experiments have verified that the ASTMS not only provides high output voltages up to 70 V, but also maintains its high voltage output over different travel distances, frequencies of movement, and contact pressures. In cyclic wind tunnel tests, the system also

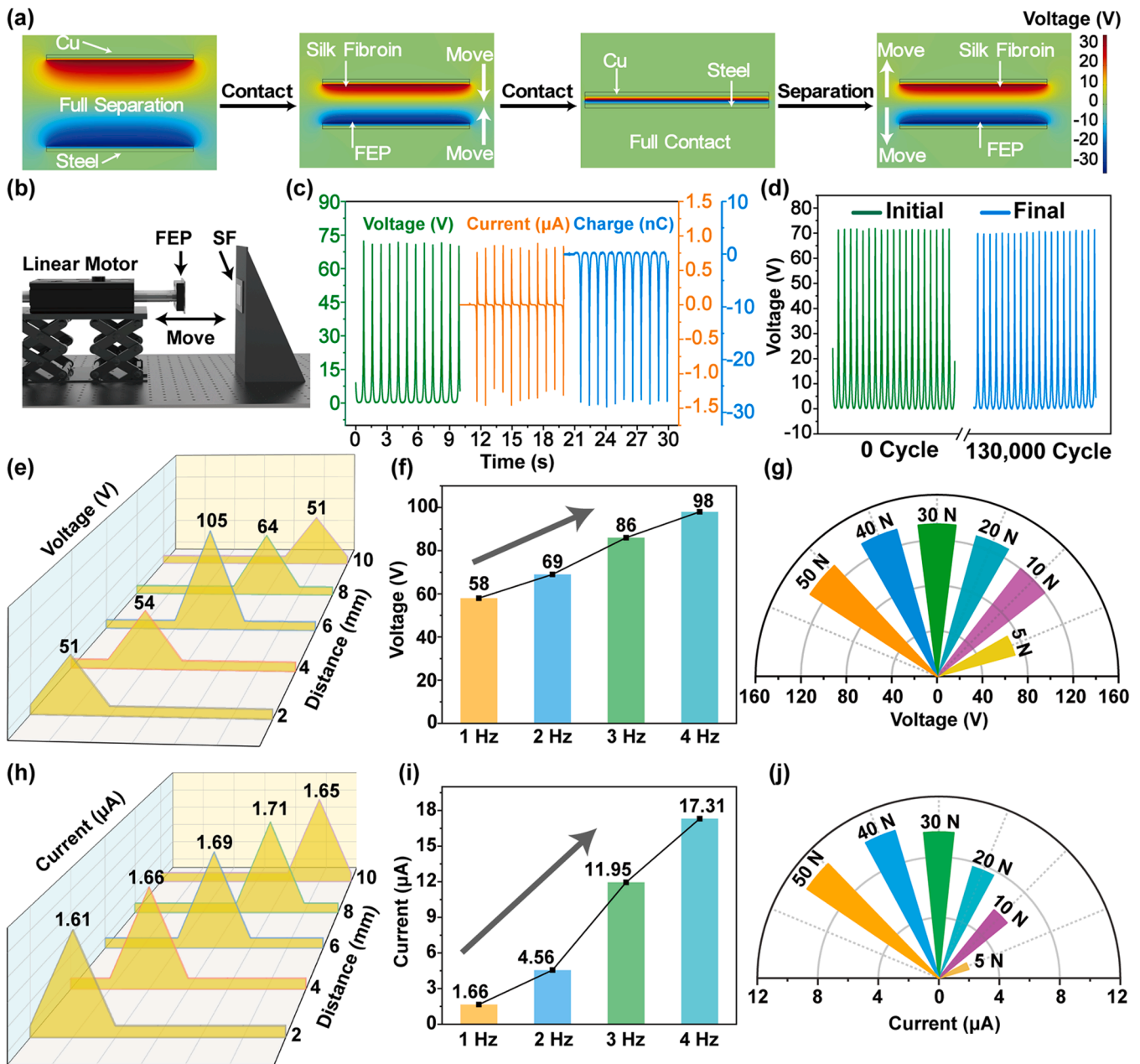


Fig. 3. ASTMS standardized triboelectric performance test. (a) Simulation of surface charge potential for contact separation mode. (b) Schematic of linear motor standardized test. (c) Output standardized test electrical properties (voltage, current, transferred charge). (d) ASTMS has been tested for durability for 130,000 cycles. (e and h) Different moving distances electrical signal output (e) voltage and (h) current. (f and i) Different moving frequencies electrical signal output (f) voltage and (i) current. (g and j) Comparison of (g) voltage output (j) current output at different contact pressures.

showed consistent high output performance. When the VG structure is placed on the NACA0012 wing motor and placed in a recirculating wind tunnel (Fig. 4h), the motor speed and the actual wind speed are shown in Table S1, and the angle of attack (AoA) of the wing is controlled by the motor in order to induce a stall state. The VG structure is placed on the surface of the airfoil, and when subjected to reverse turbulence during stall, the active electrodes begin to vibrate and separate from the SF membrane contact of the stationary electrodes, thus generating a stall sensing signal (Fig. 4a and Movie S1).

Supplementary material related to this article can be found online at [doi:10.1016/j.nanoen.2025.110694](https://doi.org/10.1016/j.nanoen.2025.110694).

When the operator receives the stall warning signal, the flight state can be adjusted in time to return the aircraft to a stable condition; once stabilized, the system stops working and the signal disappears (Fig. 4b).

Since aircraft stall states are extremely dangerous, being able to quickly and accurately recognize the flight state and having the time to adjust is critical to flight safety. The aerodynamic ultrafast response of the ASTMS based on biomimetic structure in monitoring the turbulence flow signal generated by the reverse turbulence was 0.004 s, and the signal disappeared after the recovery of the flight state was 0.006 s (Fig. 4c). Moreover, the maximum SNR of system is 56.21 dB, and the high SNR can avoid the interference caused by external environmental factors and ensure the accuracy of the signal. This aerodynamic ultrafast response time and high SNR provides fast and efficient transmission of stall signals, ensuring that the aircraft is able to make immediate adjustments to the stall and avoid over-adjustment once stable flight is restored.

At the same time, it was found in the tests that the active electrode may suffer from excessive deformation problems in the face of strong

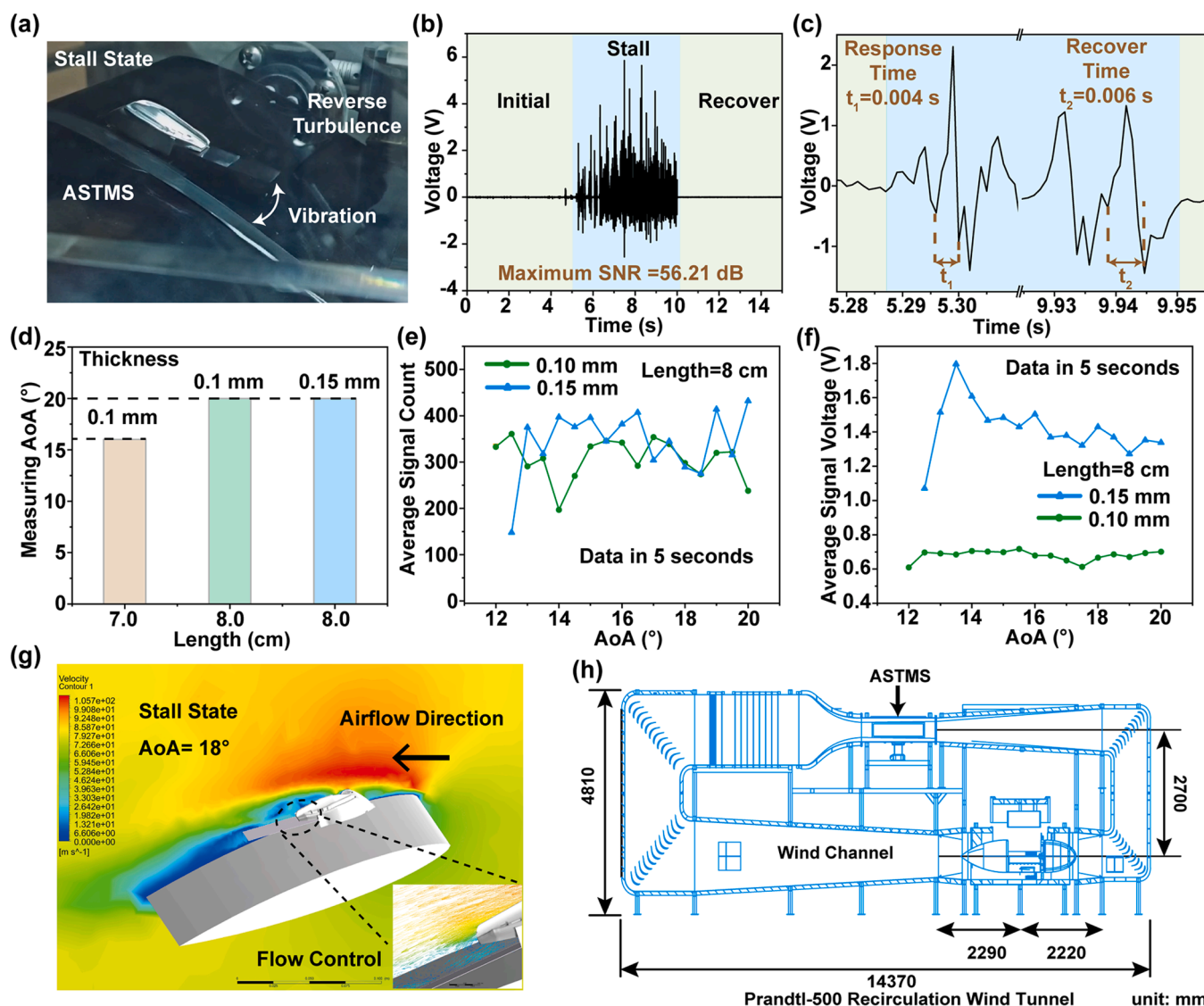


Fig. 4. Cyclic wind tunnel testing and optimization. (a) Schematic of ASTMS vibration under reverse turbulence in stall state. (b) Sensor signals of the aircraft state from normal to stall and recovery and the maximum SNR is 56.21 dB. (c) ASTMS signal response time before and after stall state. (d) Different thicknesses, lengths of active electrodes are able to measure the AoA of the signal. (e) Average signal count generated in 5 s for each AoA. (f) Average signal voltage generated over 5 s for each angle of attack. (g) Fluid-solid coupling CFD simulation of ASTMS. (h) Schematic diagram of the circulating wind tunnel structure.

reverse turbulence (Fig. S19), and this deformation may reduce the contact area between the active electrode and the stationary electrode, resulting in a weakened sensing signal. To address this issue, the inner surface and the lower surface of the VG were conformal treated (Fig. S20). First, the 304 stainless steels with a higher Young’s modulus are chosen as the material for the active electrode. The steel sheet with higher Young’s modulus has more conformal forces inside the treated VG, to ensure that there is a large contact area between the active electrode and the stationary electrode. Secondly, the ASTMS is conformal to make it fit the NACA0012 airfoil better (Fig. S21).

In addition to rapid stall monitoring, the ASTMS should be capable of stabilizing at different AoA, depending on the flight requirements. Therefore, the active electrode was optimized and different lengths and thicknesses of steel sheets were tested (length 7 cm, 8 cm, thickness 0.01 mm, 0.15 mm). Experimental results showed that the shorter active electrodes were only able to monitor AoA up to 16° and were unable to capture for higher angles (Fig. 4d). While longer active electrodes can operate at a higher range of AoA, the strength and amount of signal is also an important consideration for the sensor. The average signal counts generated by the system at different AoA were analyzed by

selecting data within 5 s (processed using MATLAB, refer to text 1 for the specific procedure) and taking multiple measurements for averaging (Fig. 4e), and it was found that the signal counts generated by the 8 cm long active electrodes were roughly similar. But a quality sensor should also have a higher SNR and be able to suppress other factors from interfering with the signal. The data within 5 s were analyzed to compare the average signal voltage (Fig. 4f), and the results showed that the 0.15 mm thick active electrode had a higher average signal voltage and SNR. Therefore, the optimized ASTMS using a 0.15 mm thick and 8 cm long steel sheet as the active electrode can obtain better sensing performance. Meanwhile, a 3D computational fluid dynamics (CFD) simulation of the ASTMS was conducted (Fig. 4g and Movie S2), and the VG with biomimetic structure can control airflow over the airfoil surface, and the setup process can be referred to Supplementary Text 2 (Figs. S22 to S31).

Supplementary material related to this article can be found online at [doi:10.1016/j.nanoen.2025.110694](https://doi.org/10.1016/j.nanoen.2025.110694).

2.5. Development of wireless transmission equipment for ASTMS signals

Although the space occupation of ASTMS is small, once the transmission line is damaged, the stall signal cannot be transmitted in time, which can seriously threaten flight safety. To address these concerns, a wireless transmission device was developed to facilitate faster and safer transmission of sensing signals from ASTMS (Fig. 5a and Fig. S32). A wireless device can reduce the amount of space used for lines in the

nacelle and can transmit signals continuously without being affected by damage to the lines. The wireless transmission device is designed to fit into less space inside the aircraft while still retaining a stable transmission capability. For signal transmission, compared to WiFi and Bluetooth transmission, a 433 MHz antenna transmits at a low frequency but has advantage of low power, long transmission distance, and weak signal decay. An adjustable transmitter was designed with reference to the data collected by the STM-32 microcontroller. The signal

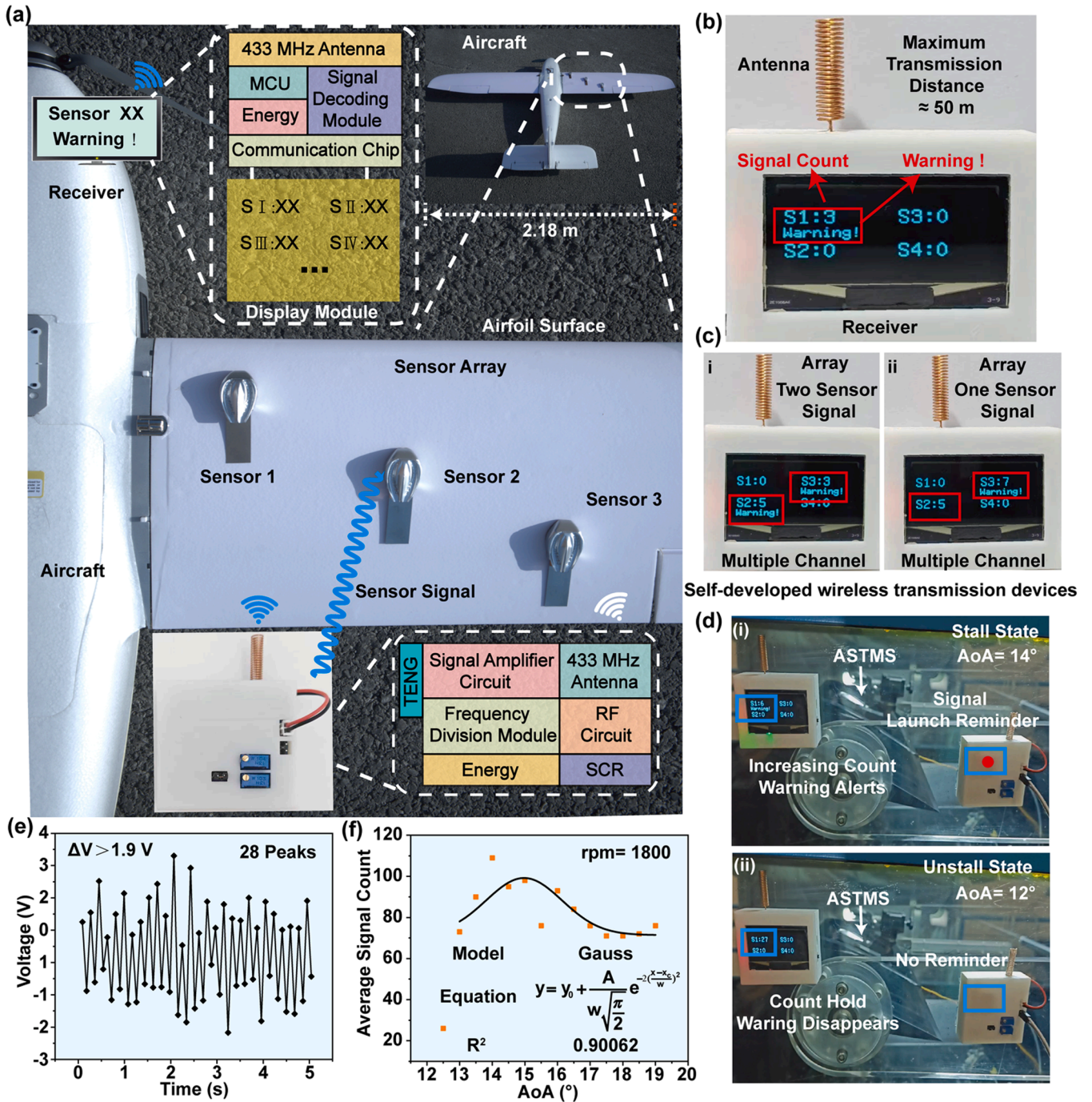


Fig. 5. Development of wireless transmission equipment for ASTMS signals. (a) Application of arrayed sensors and wireless transmission device. (b) Photograph of the warning function of the wireless receiving equipment. (c) The receiver side of the self-developed wireless transmission device can receive arrays of multiple signals and single signals. (d) Stall and un stall state wireless device states. (i) Stall state. The system signal is sent through the transmitter accompanied by a transmit reminder and an increase in the count on the receiver with a warning alert; (ii) un stall state. No signal is transmitted and the count hold at the receiver with no warning alert. (e) ASTMS monitors the signal within 5 s of the initial AoA for noise reduction. Improves the SNR of the signal while ensuring full operating status of the wireless device. (f) Noise reduction was performed on the signals over a period of 5 s at different AoA, and the number of signals after noise reduction was curve-fitted.

reference and amplification are adjusted according to the input signal and usage requirements to control the signal emission.

The receiver processes the information when it receives the signal and the display module shows the number of signals in time to warn the operator. (Fig. 5b). The wireless device has a maximum transmission distance of about 50 m, so the signal can be received at different locations on different aircraft. Once the warning was received, the operator will adjust the flight status. The warning disappears after returning to an unstall state. Notably, the wireless transmission device can transmit multiple signals (Fig. 5c). Only one receiver is required to capture signals from different transmitters. By strategically placing ASTMS at different locations on the surface of the aircraft, operators in the cockpit can continuously monitor airflow conditions to ensure the overall safety during flight.

In the cyclic wind tunnel, the ASTMS was placed in a turbulence flow by adjusting the airfoil AoA. In the stall state, the system generates sensing signals and sends them through the self-developed wireless transmission device (Fig. 5d(i) and Movie S3). The turbulence flow sensing signal is sent through the transmitter in stall state. While the signal is being transmitted, the transmitter indicator will flash once to indicate completion of a signal transmission. When the aircraft returns to a unstall state, the system stops working and no longer generates an inductive signal. At this time, the indicator light on the transmitter side stops flashing and the receiver side stops receiving signals. The warning indication on the display interface of the receiving end disappears and the aircraft returns to a safe flight state (Fig. 5d(ii)).

Supplementary material related to this article can be found online at [doi:10.1016/j.nanoen.2025.110694](https://doi.org/10.1016/j.nanoen.2025.110694).

Optimizing the turbulence flow sensing signal processing considering the characteristics of the wireless transmission device that transmits signals 5 times per second, a method to improve the SNR was applied to the signal shown in Fig. 4b. Filtering out signals below 1.9 V yields 28 high voltage peaks in 5 s (Fig. 5e). This processing not only improves the SNR but also ensures efficient operation of the transmission equipment. Using the same signal processing strategy, the SNR at different AoA was analyzed. After excluding the start and two abnormal points, curve fitting of the screened data (Fig. 5f) showed that the signals first strengthened, then weakened and stabilized as the AoA increased, indicating that the change in reverse turbulence slowed down after the AoA reached a certain value.

3. Conclusion

Monitoring of airflow status on the airfoil surface plays a vital role in the flight safety. In this paper, we present an in-situ aircraft surface turbulence mapping system with conformal, self-powered, high SNR, and biomimetic structure. Inspired by the features of manta rays, a VG with biomimetic structure is designed to control the airflow on the surface of the aircraft. Compared to traditional turbulence sensors, the ASTMS has less impact on the surface of the aircraft. Using triboelectric technology, the system provides self-powered monitoring of the airflow state and sensing without the need for external energy supply.

The exceptional SF materials have been meticulously selected as the tribomaterial for ASTMS. SF has excellent conformal ability and can be attached to the surface of objects with different morphologies, and it is robust in different environments, including high and low temperatures, acidic and alkaline, and humid environments. In addition, SF is a strong positive tribomaterial, which can generate sensing signals at the volt level, the system has aerodynamic ultrafast response and maximum SNR can reach 56.12 dB, effectively minimizing external interference.

The results from cyclic wind tunnel tests affirm that ASTMS can promptly generate sensing signals during stall events, with the signals disappearing immediately after recovery. Furthermore, the system exhibits exceptional monitoring capabilities across a wide range of AoA. Moreover, we have self-developed a set of wireless transmission equipment. The sensing signal of the system is transmitted through a 433 MHz

antenna, which transmits a more stable signal and consumes less power. In the event of turbulence on the surface of the aircraft, the ASTMS works to generate a signal that is sent to the control room via a wireless device to make a stall warning alert to the operator. The pairing of ASTMS with wireless device reduces the difficulty of scheduling and allows it to be placed at various locations on the surface of the aircraft for distributed sensing. The flight safety of the aircraft is further ensured by the monitoring of the airflow status in more locations.

4. Experimental and methods section

4.1. Integration of ASTMS

The system consists of four main components: the VG support structure, the stationary electrodes, the movable electrodes, and the wireless transmission device for sensing signals. In this study, it was considered that the modification of the surface of the aircraft would affect the safety of the aircraft. Therefore, the VG structure on the surface of the aircraft was modified with as little impact on the safety of the aircraft as possible.

In previous work, there was a question as to whether the sensor would cause damage to the surface of the aircraft, which was also avoided in this study. The active electrodes leave the surface of the aircraft when the sensor is in operation and rest on the surface of the aircraft when it stops working, and do not cause damage to the surface of the aircraft. The stationary electrode section applies the SF membrane used in previous work, which is capable of generating a higher sensing signal during contact separation. The active electrode section was explored as it is directly responsive to the airflow state on the surface of the aircraft. The more readily available materials copper and 304 stainless steel (20 mm wide) were chosen. Because of the different materials and the different weights of the two materials under the same conditions, different types of active electrodes were tested for their behavior under airflow (0.1 mm thick, 0.15 mm thick, 50–80 mm in length).

Due to the difference in Young's modulus of the materials, copper at the same thickness can undergo excessive deformation during operation, which may affect the surface airflow state of the aircraft. At the same time, excessive deformation would make incomplete contact between the active electrode and the stationary electrode inside the VG structure. This results in a weak sensing signal, or a high noise level and a low SNR. Therefore, the steel with a higher Young's modulus is chosen as the active electrode. It is not only possible to work without large deformation, but it will not affect the airflow state on the surface of the aircraft. At the same time, it can obtain a higher contact area with the static electrode, higher sensing signal, and SNR.

4.2. Cyclic wind tunnel testing

In the present work, we performed a series of tests related to ASTMS in a cyclic wind tunnel (Prandtl-500). The overall length of the wind tunnel is 14.4 m and the height is 4.8 m. The working section is a rectangular space with a length of 2 m and a length and width of 500 mm. At the bottom of the working section, it is possible to install test equipment and so on. Three sides of the working section are made of transparent glass so that the experiments can be well observed. To minimize boundary layer effects in the region of the working section, a 1.9-meter-long neck section is also configured in front of and behind the working section. To ensure a stable laminar flow in the test section, it is equipped with a 2.6-meter-long filter section, so that the circulating airflow becomes laminar as it flows into the working section. The maximum wind speed of the cyclic wind tunnel can reach 80 m per second. The degree of turbulence of the incoming flow as well as the rate of change of wind speed in the cross-section of the working section are negligible. The turbulence is less than 0.2 % and the rate of change is less than 0.5 %. In addition, to more accurately verify the performance

of the ASTMS in a cyclic wind tunnel, different AoA of the aircraft were simulated by stepper motors to manipulate the simulation, with an accuracy of 0.1 degree of AoA variation.

4.3. Experimental data collection

A series of tests for the validation of the ASTMS in this study used two data collection methods. A Keithley 6514 electrometer was used for the standardized validation data acquisition, and a low-power STM-32 microcontroller used in previous work was used for the cyclic wind tunnel data testing. Wind tunnel test signals are collected using a low-power STM-32 microcontroller. In addition to collecting signals wirelessly, the STM-32 microcontroller can adjust the baseline of the sensed signals. This is different from the way the Keithley 6514 electrometer signals are captured, where the STM-32 microcontroller captures signals that are closer to the signals that are imported into the external circuit.

4.4. Self-research wireless transmission equipment

In tests conducted in the cyclic wind tunnel, the frequency of TENG signal triggering was found to be high, reaching dozens of signal triggers per second. The TENG signal undergoes processing by transmitter and receiver circuits before achieving wireless transmission and reception (Figs. S33 and S34). In this process, the TENG signal from the access circuit is initially amplified and processed by the crossover module, sending the signal to the silicon-controlled rectifier (SCR) module. The SCR module then takes the received TENG signal, converts it to a high level, and activates the circuit to transmit the signal. This transformation of the TENG signal, known for its short response time, into a high-level signal enables the activation of circuit operation. Simultaneously, adjusting the threshold for SCR triggering allows control over the transmit frequency. The activated circuitry processes the data through radio frequency (RF) circuitry and transmits it through a 433 MHz antenna. Similarly, at the receiving end, the 433 MHz antenna receives signals from the transmitter, decodes them, and displays them on the display module (refer to text 3).

4.5. Characterization and measurements

In this study, the standardized test of ASTMS was done with a linear motor. The linear motor used is LinMot E1100 (Kerry Linmot (Suzhou) Co., Ltd.). The collection of standardized experimental data is done through Keithley 6517. By completing high wind speed tests in a wind tunnel. The wind tunnel tests in this work use the Prandtl-500 cyclic wind tunnel (Tianjin Prandtl Co., Ltd.). Different AoA is controlled by stepper motors with a chord length of 20 cm (Cangzhou Kederuier Experimental Equipment Co., Ltd.). Wind tunnel test data acquisition via low-power STM-32 microcontroller (self-developed program). Self-developed wireless transmission device are completed with Altium Designer software and printed onto printed circuit board through commercial factories (Shenzhen Jialichuang Technology Group Co., Ltd.). The silk fibroin membranes were tested by means of a Fourier transform infrared spectrometer (FTIR) (made by the German manufacturer Bruker, instrument model VERTEX80v).

CRediT authorship contribution statement

Xu Zijie: Writing – review & editing, Supervision, Project administration, Funding acquisition, Conceptualization. **Guo Wenxi:** Writing – review & editing, Supervision. **Chen Baodong:** Supervision, Funding acquisition. **Tang Wei:** Supervision. **Li Chengyu:** Software, Data curation. **Shang Yurui:** Software, Investigation. **Cao Leo N.Y.:** Writing – review & editing, Methodology, Data curation. **Fang Zhong Lin:** Writing – review & editing, Supervision, Resources, Funding acquisition, Conceptualization. **Sheng Hengrui:** Writing – original draft, Software, Formal analysis, Data curation, Conceptualization. **Sun Yanshuo:**

Writing – review & editing, Conceptualization. **Jiang Yang:** Writing – review & editing. **Zhou Zhuayu:** Visualization, Validation, Methodology, Formal analysis, Data curation.

Declaration of Competing Interest

The authors declare that they have no known competing financial interests or personal relationships that could have appeared to influence the work reported in this paper.

Acknowledgments

This research was supported by the National Natural Science Foundation of China (Grant No. 52203324); National Key R&D Program of China (2023YFB2604600); National Key R&D Project from the Minister of Science and Technology (2021YFA1201601). Thanks to the Georgia Institute of Technology for providing software support.

Appendix A. Supporting information

Supplementary data associated with this article can be found in the online version at [doi:10.1016/j.nanoen.2025.110694](https://doi.org/10.1016/j.nanoen.2025.110694).

Data availability

Data will be made available on request.

References

- [1] C. Huang, Further improving general aviation flight safety: analysis of aircraft accidents during takeoff, *Coll. Aviat. Rev. Int.* 38 (2020) 88–105, <https://doi.org/10.22488/okstate.20.100206>.
- [2] T. Dong, Q. Yang, N. Ebadi, X.R. Luo, P. Rad, Identifying incident causal factors to improve aviation transportation safety: proposing a deep learning approach, *J. Adv. Transp.* 2021 (2021) 5540046, <https://doi.org/10.1155/2021/5540046>.
- [3] M. Raissi, A. Yazdani, G.E. Karniadakis, Hidden fluid mechanics: learning velocity and pressure fields from flow visualizations, *Science* 367 (2020) 1026–1030, <https://doi.org/10.1126/science.aaw4741>.
- [4] V. Spandan, D. Putt, R. Ostilla-Mónico, A.A. Lee, Fluctuation-induced force in homogeneous isotropic turbulence, *Sci. Adv.* 6 (2020) 0461, <https://doi.org/10.1126/sciadv.aba0461>.
- [5] M. Garcia-Sanz, Control Co-Design: an engineering game changer, *Adv. Control Appl.* 1 (2019) 18, <https://doi.org/10.1002/adc.2.18>.
- [6] C. Ming, X. Wang, A novel linear active disturbance rejection control design for air-breathing supersonic vehicle attitude system with prescribed performance, *Int. J. Aerosp. Eng.* 2020 (2020) 1676739, <https://doi.org/10.1155/2020/1676739>.
- [7] H. Zhao, K. Peng, Z. Wu, W. Zhang, J. Yang, J. Sun, Numerical simulation of supersonic carman curve bodies with aerospike, *Int. J. Aerosp. Eng.* 2021 (2021) 8821721, <https://doi.org/10.1155/2021/8821721>.
- [8] K.A. Weidenmann, E. Kerscher, T. Hammers, Mechanical properties of compound extruded aircraft stringer profiles under cyclic loading, *Adv. Eng. Mater.* 12 (2010) 584–586, <https://doi.org/10.1002/adem.200900327>.
- [9] N. Cartocci, M.R. Napolitano, G. Costante, P. Valigi, M.L. Fravolini, Aircraft robust data-driven multiple sensor fault diagnosis based on optimality criteria, *Mech. Syst. Signal Pr.* 170 (2022) 108668, <https://doi.org/10.1016/j.ymsp.2021.108668>.
- [10] S. Fuller, Z. Yu, Y.P. Talwekar, A gyroscope-free visual-inertial flight control and wind sensing system for 10-mg robots, *Sci. Robot.* 7 (2022) 8184, <https://doi.org/10.1126/scirobotics.abq8184>.
- [11] J.H. Marks, Trust in crises and crises of trust, *Hastings Cent. Rep.* 53 (2023) S9–S15, <https://doi.org/10.1002/hast.1518>.
- [12] S. Grigg, R. Pullin, C. Featherston, Acoustic emission source location in complex aircraft structures using three closely spaced sensors, *Mech. Syst. Signal Pr.* 164 (2022) 108256, <https://doi.org/10.1016/j.ymsp.2021.108256>.
- [13] M.H. Hamza, R. Polichshuk, H. Lee, P. Parker, A. Campbell, A. Chattopadhyay, Aircraft post-upset flight risk region prediction for aviation safety management, *Adv. Eng. Inform.* 54 (2022) 101804, <https://doi.org/10.1016/j.aei.2022.101804>.
- [14] Y.W. Chin, J.M. Kok, Y.Q. Zhu, W.L. Chan, J.S. Chahl, B.C. Khoo, G.K. Lau, Efficient flapping wing drone arrests high-speed flight using post-stall soaring, *Sci. Robot.* 5 (2020) 2386, <https://doi.org/10.1126/scirobotics.aba2386>.
- [15] Y. Liu, Z. Liu, A. Huang, J. Wang, C. Xin, Theoretical modeling and simulation of fiber bragg grating sensor interrogator based on linear variable filter, *Opt. Express* 31 (2023) 5777–5793, <https://doi.org/10.1364/OE.475654>.
- [16] J.K. Sahota, N. Gupta, D. Dhawan, Fiber bragg grating sensors for monitoring of physical parameters: a comprehensive review, 060901-060901, *Opt. Eng.* 59 (2020), <https://doi.org/10.1117/1.OE.59.6.060901>.

- [17] Y. Liu, Z. Jing, Q. Liu, A. Li, C.A. Teng, Y. Cheung, A. Lee, F. Tian, W. Peng, Differential-pressure fiber-optic airflow sensor for wind tunnel testing, *Opt. Express* 28 (2020) 25101–25113, <https://doi.org/10.1364/OE.401677>.
- [18] F. Li, G. Lin, X. Lu, L. Song, Enhancement of insensitivity for pitot-static probe by static-pressure orifices optimization, *IEEE Trans. Instrum. Meas.* 71 (2022) 1–8, <https://doi.org/10.1109/TIM.2022.3162267>.
- [19] H. Kwon, Y. Park, J.H. Kim, C.G. Kim, Embedded fiber bragg grating sensor-based wing load monitoring system for composite aircraft, *Struct. Health Monit.* 18 (2019) 1337–1351, <https://doi.org/10.1177/1475921719843772>.
- [20] Q. He, W. Zhang, P. Lu, J. Liu, Performance comparison of representative model-based fault reconstruction algorithms for aircraft sensor fault detection and diagnosis, *Aerosp. Sci. Technol.* 98 (2020) 105649, <https://doi.org/10.1016/j.ast.2019.105649>.
- [21] G. Yan, T. Wang, L. Zhu, F. Meng, W. Zhuang, A novel strain-decoupled sensitized FBG temperature sensor and its applications to aircraft thermal management, *Opt. Laser Technol.* 140 (2021) 106597, <https://doi.org/10.1016/j.optlastec.2020.106597>.
- [22] Y. Wang, L. Qiu, Y. Luo, R. Ding, F. Jiang, A piezoelectric sensor network with shared signal transmission wires for structural health monitoring of aircraft smart skin, *Mech. Syst. Signal Pr.* 141 (2020) 106730, <https://doi.org/10.1016/j.ymsp.2020.106730>.
- [23] K. Bednarska, P. Sobotka, T.R. Woliński, O. Zakręcka, W. Pomianek, A. Nocoń, P. Lesiak, Hybrid fiber optic sensor systems in structural health monitoring in aircraft structures, *Materials* 13 (2020) 2249, <https://doi.org/10.3390/ma13102249>.
- [24] H. Sheng, L.N. Cao, C. Li, Z. Zhou, Y. Jiang, Y. Sun, B. Chen, Z. Xu, Z.L. Wang, Self-powered digital angle sensor based on triboelectric signal for variable structure of aircraft, *Adv. Mater. Technol.* 9 (2024) 2301708, <https://doi.org/10.1002/admt.202301708>.
- [25] Z. Zhou, Z. Xu, L.N. Cao, H. Sheng, C. Li, Y. Shang, W. Tang, Z.L. Wang, Triboelectricity based self-powered digital displacement sensor for aircraft flight actuation, *Adv. Funct. Mater.* 34 (2024) 2311839, <https://doi.org/10.1002/adfm.202311839>.
- [26] L.N. Cao, Z. Xu, Z.L. Wang, Application of triboelectric nanogenerator in fluid dynamics sensing: past and future, *Nanomaterials* 12 (2022) 3261, <https://doi.org/10.3390/nano12193261>.
- [27] E. Su, H. Li, J. Zhang, Z. Xu, B. Chen, L.N. Cao, Z.L. Wang, Rationally designed anti-glare panel arrays as highway wind energy harvester, *Adv. Funct. Mater.* 33 (2023) 2214934, <https://doi.org/10.1002/adfm.202214934>.
- [28] Y. Sun, C. Li, Z. Xu, Y. Cao, H. Sheng, Z.L. Wang, L.N. Cao, Conformable multifunctional space fabric by metal 3D printing for collision hazard protection and self-powered monitoring, *ACS Appl. Mater. Inter.* 15 (2023) 57726–57737, <https://doi.org/10.1021/acsami.3c15232>.
- [29] W. Zhang, G. Gu, Z. Zhang, H. Ren, H. Zhou, Y. Gui, Z. Du, G. Cheng, Enhancing the output energy of triboelectric nanogenerator by adaptive arc discharge devices and its application in wireless weather sensing system, *Nano Energy* 129 (2024) 109987, <https://doi.org/10.1016/j.nanoen.2024.109987>.
- [30] Z. Zhang, G. Gu, W. Zhang, Z. Du, G. Cheng, Triboelectric nanogenerator with enhanced charge density and limited open-circuit voltage for efficient power management and industrial environmental monitoring, *Nano Energy* 131 (2024) 110308, <https://doi.org/10.1016/j.nanoen.2024.110308>.
- [31] K. Tao, J. Yu, J. Zhang, A. Bao, H. Hu, T. Ye, Q. Ding, Y. Wang, H. Lin, J. Wu, Deep-learning enabled active biomimetic multifunctional hydrogel electronic skin, *ACS nano* 17 (2023) 16160–16173, <https://doi.org/10.1021/acsnano.3c05253>.
- [32] M. Wu, Z. Shao, N. Zhao, R. Zhang, G. Yuan, L. Tian, Z. Zhang, W. Gao, H. Bai, Biomimetic, knittable aerogel fiber for thermal insulation textile, *Science* 382 (2023) 1379–1383, <https://doi.org/10.1126/science.adj8013>.
- [33] M. Algan, M. Seyhan, M. Sarioğlu, Effect of aero-shaped vortex generators on NACA 4415 airfoil, *Ocean Eng.* 291 (2024) 116482, <https://doi.org/10.1016/j.oceaneng.2023.116482>.
- [34] P. Gong, E.J. Aju, Y. Jin, On the aerodynamic loads and flow statistics of airfoil with deformable vortex generators, *Phys. Fluids* 34 (2022), <https://doi.org/10.1063/5.0092187>.
- [35] E. Milana, R. Zhang, M.R. Vetrano, S. Peerlinck, M. De Volder, P.R. Onck, D. Reynaerts, B. Gorissen, Metachronal patterns in artificial cilia for low reynolds number fluid propulsion, *Sci. Adv.* 6 (2020) 2508, <https://doi.org/10.1126/sciadv.abd2508>.
- [36] M. Mani, A.J. Dorgan, A perspective on the state of aerospace computational fluid dynamics technology, *Annu. Rev. Fluid Mech.* 55 (2023) 431–457, <https://doi.org/10.1146/annurev-fluid-120720-124800>.
- [37] J.L. Callahan, G. Rigas, J.C. Loiseau, S.L. Brunton, An empirical mean-field model of symmetry-breaking in a turbulent wake, *Sci. Adv.* 8 (2022) 4786, <https://doi.org/10.1126/sciadv.abm4786>.
- [38] Y. Liu, Z. Liu, A. Huang, J. Wang, C. Xin, Theoretical modeling and simulation of fiber bragg grating sensor interrogator based on linear variable filter, *Opt. Express* 31 (2023) 5777–5793, <https://doi.org/10.1364/OE.475654>.
- [39] M.A. Saputra, N.I. Supardi, A. Suandi, Aerodynamic characteristics of amphibian aircraft using computational fluid dynamics (CFD) method, *Rekayasa Mek.* 1 (2023) 1–6, <https://doi.org/10.33369/rekayamekanika.v7i1.30097>.
- [40] A. Alexakis, R. Marino, P.D. Mininni, A. van Kan, R. Foldes, F. Feraco, Large-scale self-organization in dry turbulent atmospheres, *Science* 383 (2024) 1005–1009, <https://doi.org/10.1126/science.adg8269>.
- [41] A. Ji, X. Luo, X. Yang, A multistimuli-responsive recyclable poly(vinyl alcohol)/perylene imide hydrogel of high-performance piezoresistive sensors for human wearable devices, *J. Appl. Polym. Sci.* 141 (2024) 55595, <https://doi.org/10.1002/app.55595>.
- [42] R. Jiang, J. Pu, Y. Wang, J. Chen, G. Fu, X. Chen, J. Yang, J. Shen, X. Sun, J. Ding, X. Xu, Tailored wrinkles for tunable sensing performance by stereolithography, *Interdiscip. Mater.* 3 (2024) 414–424, <https://doi.org/10.1002/idm2.12161>.
- [43] S. Ören, O. Özbeke, Ö. İslidak, The use of thiazole derivative molecules as sensor materials: potentiometric determination of Cu(II) ions, *Vietnam J. Chem.* 62 (2024) 486–492, <https://doi.org/10.1002/vjch.202300295>.
- [44] R. Qin, J. Nong, K. Wang, Y. Liu, S. Zhou, M. Hu, H. Zhao, G. Shan, Recent Advances in flexible pressure sensors based on MXene materials, *Adv. Mater.* 36 (2024) 2312761, <https://doi.org/10.1002/adma.202312761>.
- [45] H. Lu, J. Wang, J. Li, B. Gao, B. He, Advanced silk fibroin biomaterials-based microneedles for healthcare, *Macromol. Biosci.* 23 (2023) 2300141, <https://doi.org/10.1002/mabi.202300141>.
- [46] L.M. Lopes, G.Y. Ottaiano, L. de Souza Guedes, M.A. de Moraes, M.M. Beppu, Analyzing the interactions and miscibility of silk fibroin/mucin blends, *J. Appl. Polym. Sci.* 141 (2024) e55343, <https://doi.org/10.1002/app.55343>.
- [47] Z. Xu, L.N. Cao, C. Li, Y. Luo, E. Su, W. Wang, W. Tang, Z. Yao, Z.L. Wang, Digital mapping of surface turbulence status and aerodynamic stall on wings of a flying aircraft, *Nat. Commun.* 14 (2023) 2792, <https://doi.org/10.1038/s41467-023-38486-6>.

Glossary

Field-specific terms: Definition

TENGs: triboelectric nanogenerators

TENG: triboelectric nanogenerator

VG: vortex generator

ASTMS: aircraft surface turbulence mapping system

FEP: fluorinated ethylene propylene

SF: silk fibroin

AFM: atomic force microscopy

SNR: signal-to-noise ratio

CFD: computational fluid dynamics

SCR: silicon-controlled rectifier

RF: radio frequency



Hengrui Sheng received his M.S. degree from Guangxi University in 2024 and is currently pursuing a Ph.D. degree at Beijing Institute of Nanoenergy and Nanosystems, Chinese Academy of Sciences. His main research interests include digital sensing of aircraft safety parameters based on triboelectric effect and sensing of fluid-related parameters.



Leo N.Y. Cao received his Ph.D. degree from the University of Minnesota in 2017 and is currently an associate professor at Beijing Institute of Nanoenergy and Nanosystems, Chinese Academy of Sciences. His research interests include the exploration of energy harvesting and sensing in the field of fluid mechanics using TENG.



Yurui Shang received his M.S. degree from Guangxi University in 2024 and is currently pursuing a Ph.D. degree at Beijing Institute of Nanoenergy and Nanosystems, Chinese Academy of Sciences. His research interests include nonpower energy harvesting, the power management circuit of TENG, and embedded development.



Chengyu Li received the Ph.D. degree from the University of Chinese Academy of Sciences in 2024 and is currently working at the Hong Kong Polytechnic University. His research interests include TENG applications in flexible wearables and energy harvesting management.



Baodong Chen received her Ph.D. degree from Inner Mongolia University of Technology in 2015 and is currently a professor at Beijing Institute of Nanoenergy and Nanosystems, Chinese Academy of Sciences. He main research interests include micro and nano energy harvesting and self-powered sensing systems.



Zhu Yu Zhou received his M.S. degree from Zhejiang Normal University in 2024 and he worked at the Beijing Institute of Nanoenergy and Nanosystems. His main research interests are micro and nano energy harvesting and sensing applications of TENG.



Wenxi Guo received his Ph.D. degree from Xiamen University in 2014 and is currently a professor at the School of Physical Science and Technology of Xiamen University. His research includes the preparation of flexible materials, flexible electronics, and degradable sensors.



Yang Jiang received her Ph.D. degree from the University of Chinese Academy of Sciences in 2022 and is currently an associate professor at Beijing Institute of Nanoenergy and Nanosystems, Chinese Academy of Sciences. Her research interests include self-powered sensing and self-powered systems using the TENG.



Zijie Xu received his Ph.D. degree from Xiamen University in 2021 and is currently an associate professor at Beijing Institute of Nanoenergy and Nanosystems, Chinese Academy of Sciences. His research interests include intelligent fluid dynamics sensing systems; flexible functional materials; flexible self-powered electronic system.



Yanshuo Sun received her M.S. degree from Guangxi University in 2022 and is currently pursuing the Ph.D. degree in Beijing Institute of Nanoenergy and Nanosystems, Chinese Academy of Sciences, China. Her current research interests include self-powered sensing in extreme environments.



Zhong Lin Wang received his Ph.D. in physics from Arizona State University in 1987. He is currently the director of the Beijing Institute of Nanoenergy and Nanosystems, Chinese Academy of Sciences. He established the TENG field and his research includes TENG energy harvest and self-powered systems.



Wei Tang received her Ph.D. degree from the Peking University in 2013 and is currently a professor at Beijing Institute of Nanoenergy and Nanosystems, Chinese Academy of Sciences. Her research interests include TENG applications in wearable and self-actuated sensing.